R.E.M. (Rekayasa Energi Manufaktur) Jurnal | Vol.11 No.1/2026
ISSN online (2528-3723)
http://doi.org/10.21070/rem.v11i1.1840

Effect of Flow Disturbance Geometry on Thermal Hydraulic Performance of Forced Air-Cooled Heat Sinks for CPU Cooling

Annisa Fitriola Suryawati[1], Damora Rhakasywi[1], Nicky Yongkimandalan[1], Bima Rakha Adhitama[1]
Email corresponding author: rhakasywi@upnvj.ac.id

[1] Mechanical Engineering Department, Faculty of Engineering, Universitas Pembangunan Nasional Veteran Jakarta, Jl. Limo Raya No.80, Limo, Kota Depok, Jawa Barat, 16514, Indonesia

Article history: Received: 8 May 2026 | Revised: 29 May 2026 | Accepted: 31 May 2026

Abstract. *The increasing thermal load in modern electronic devices necessitates efficient and reliable cooling strategies, particularly for air-cooled heat sinks in CPU applications. This study numerically investigates the effect of flow-disturbance geometry on the thermal–hydraulic performance of a forced air-cooled channel under constant heat flux. Three configurations—circular, square, and octagonal—were evaluated against a baseline using a validated CFD approach based on the RANS equations with the k–ω SST model, with a 7.65% deviation. The results show that geometric disturbances significantly influence temperature distribution and pressure drop. The octagonal model achieves the lowest excess temperature across airflow velocities of 1–2 m/s but produces the highest pressure drop, while the square model provides notable temperature reduction with moderate pressure loss by improving airflow uniformity and disrupting the thermal boundary layer. Overall, the square configuration offers the most optimal balance between heat transfer and energy efficiency.*

Keywords – *CPU Cooling; heat sinks; temperature*

INTRODUCTION

The rapid increase in power density in modern electronic devices, such as CPUs and power modules, has significantly intensified the demand for effective thermal management systems to ensure operational reliability and sustained performance [1]. Excessive heat generation can accelerate thermal degradation, reduce system efficiency, and shorten the lifespan of electronic components [2]. To address these challenges, various cooling strategies have been developed, including passive air cooling [3], forced-air cooling, liquid cooling [4], phase-change methods [5], and hybrid cooling techniques [6]. Among these approaches, air-cooled heat sinks remain widely used in electronic cooling applications due to their simple design, cost-effectiveness, ease of integration, and low maintenance requirements compared to more complex solutions such as liquid cooling systems [7]. The thermal performance of heat sinks is strongly influenced by geometric parameters, including fin height, spacing, and thickness, as well as airflow conditions [8]. Previous studies have shown that airflow characteristics, such as the fan inlet impingement angle, can significantly affect thermal performance, where simplified assumptions like uniform impingement may underestimate the actual base temperature by approximately 16% [1]. Another strategy to enhance cooling performance involves modifying the internal channel configuration, such as implementing mini-channel heat sinks, which have demonstrated significant reductions in peak temperature, reaching up to 34.1 °C [2]. Despite these improvements, further geometric and flow-control modifications are still required to enhance the effectiveness of air-cooling systems and meet the increasing thermal demands of modern electronic devices.

Approaches to improving heatsink cooling performance have included several liquid-based methods. A previous study on liquid cooling reported that Al2O3/Water and SiC nanofluids improved heatsink cooling performance by only 2–3%, indicating limited enhancement in convective heat transfer compared to the additional system complexity introduced [9]. Another study showed that nanofluid velocity and the geometry of the heat-source attachment area significantly affected heatsink thermal performance [10]. Increasing nanofluid velocity reduced the average heatsink temperature, while the connection length between the LED and the heatsink strongly influenced the maximum temperature distribution, demonstrating that cooling effectiveness remained highly dependent on operating conditions and system configuration. In addition to liquid cooling, phase-change cooling methods using PCM with metal-oxide nanoparticles (Al2O3, SiO2, and TiO2) have also been investigated [11]. The study reported surface-temperature reductions of 8–15 °C and a maximum efficiency improvement of 9.2% compared to uncooled conditions. However, the enhancement remained relatively moderate considering the increased material requirements, thermal-storage limitations, and operational complexity associated with PCM integration.

Although liquid cooling, PCM cooling, and hybrid thermal-management techniques have demonstrated measurable improvements in heat-dissipation capability, their implementation generally requires more complex

systems, higher manufacturing costs, and additional maintenance. Therefore, despite the development of advanced cooling techniques, air-cooled heatsinks continue to be widely used because of their lower cost, simpler configuration, and better compatibility with compact electronic systems. Nevertheless, further improvements are still required to satisfy the increasing thermal-management demands of electronic devices, especially since many previous studies reported only limited temperature reductions despite employing more complex cooling approaches. One promising method to improve the thermal performance of air-cooled heatsinks is the introduction of flow-disturbance mechanisms. Such modifications can enhance airflow mixing, and improve convective heat transfer around the heatsink surfaces without significantly increasing system complexity. Therefore, the present study investigates the capability of an air-cooling system to dissipate a prescribed heat flux through flow-disturbance modifications. The findings are expected to provide further insight into the effectiveness of airflow-manipulation strategies for improving the thermal performance of air-cooled heatsinks while maintaining a simpler and more economically feasible cooling configuration compared with previously reported advanced cooling methods.

METHODS

A. Geometry and Boundary Conditions

Referring to the previous study by Yu Li et al. [12], the model geometry and boundary conditions used in the present study were developed to represent an air-cooling configuration under a constant heat-flux condition. The computational domain consists of a rectangular cooling channel designed to simulate airflow passing over a heated surface. The geometry includes the main channel length (L), channel height (H), jet length (L_{jet}), and channel height (H_{ch}), which were selected based on typical dimensions used in compact electronic cooling applications. These parameters were carefully defined to ensure that the airflow distribution within the channel accurately represents forced-convection conditions commonly encountered in air-cooled thermal management systems. The detailed geometric dimensions used in the numerical model are summarised in Table 1 and Figure 1. These parameters include the channel width (W), channel length (L), and channel height (H), which serve as the primary references for constructing the computational domain. The selected dimensions ensure consistency with previously validated numerical configurations while allowing the investigation of airflow behaviour under modified flow conditions. This approach enables a systematic evaluation of the influence of flow-disturbance structures on the thermal performance of the air-cooling configuration.

Table 1. Geometry specification details

Details	Size *(mm)*
W	1.5
L	60.5
L_{jet}	45
H	23.9
H_{ch}	10

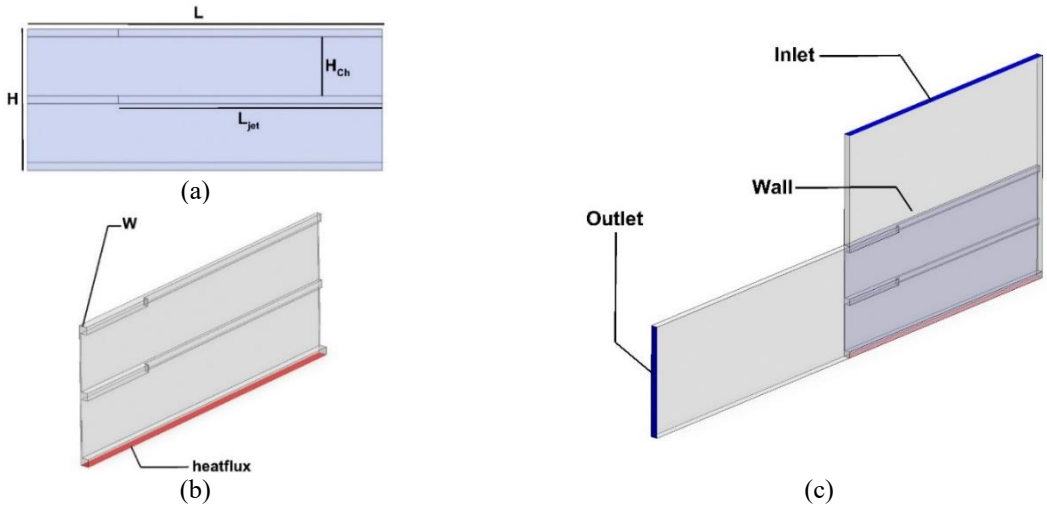

Figure 1. Model geometry details (a) 2D Baseline geometry details, (b) 3D Baseline geometry details, and (c) computational domain of the configuration.

In this study, a flow-disturbance modification was incorporated into the cooling channel to intensify airflow mixing and enhance convective heat transfer under a constant heat-flux condition. The disturbance elements were strategically placed within the channel to increase local turbulence, redistribute the airflow pattern, and reduce the thickness of the thermal boundary layer adjacent to the heated surface. By disrupting the formation of a stable boundary layer along the channel walls, these structures are expected to strengthen the interaction between the airflow and the heat-transfer surface, thereby improving the overall cooling performance. To systematically examine the effect of disturbance geometry on airflow behavior and thermal characteristics, three different configurations were evaluated, namely square, circular, and octagonal shapes, as depicted in Figures 2(a), 2(b), and 2(c), respectively. All configurations were positioned identically within the channel to ensure a fair comparison and to isolate the influence of geometric variation. These geometrical modifications were designed to assess their capability in altering flow structures and promoting more uniform airflow distribution within the cooling channel. Achieving better airflow uniformity is crucial in forced convection systems, as non-uniform flow can result in localized hot spots and degrade overall thermal performance.

Furthermore, the presence of these disturbance elements is expected to generate secondary flow structures, increase local mixing intensity, and promote stronger interaction between the working fluid and the heated surface. Differences in geometric shape are also anticipated to influence the strength of flow separation, recirculation zones, and wake formation downstream of the disturbance elements. Therefore, a comparative evaluation of square, circular, and octagonal disturbance geometries provides a systematic approach to understanding their effectiveness in improving airflow uniformity and enhancing the convective heat-transfer capability of the proposed air-cooling channel configuration. In addition, these geometric variations may significantly affect the pressure drop characteristics within the channel, which directly influence the required fan power and overall energy efficiency of the system. Geometries that induce stronger turbulence typically enhance heat transfer but also introduce higher flow resistance, leading to increased energy consumption. Conversely, milder disturbances may reduce pressure penalties but provide limited thermal improvement. Therefore, evaluating both thermal and hydraulic responses is essential to identify an optimal configuration that balances enhanced heat transfer performance with acceptable energy requirements for practical engineering applications.

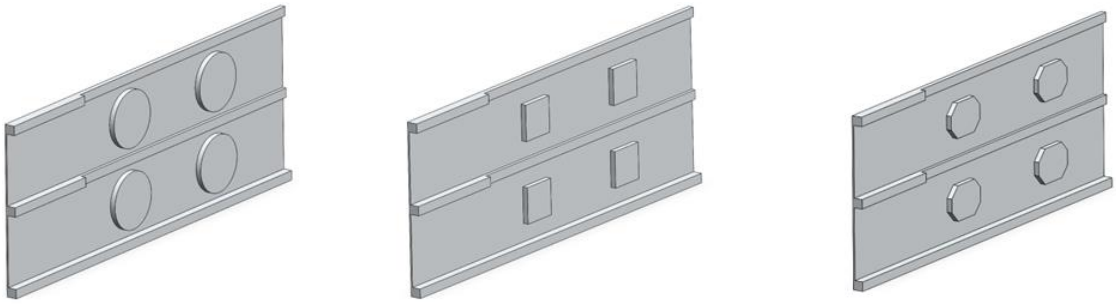

(a) (b) (c)

Figure 2. Modified geometries (a) Model 1, (b) Model 2, and (c) Model 3.

B. Meshing Refinement

To effectively capture the complex geometry of the cooling system, the computational domain was discretised using an unstructured tetrahedral mesh and a structured mesh for the domain. This meshing strategy provides flexibility and accurate representation of the surfaces. Figure 3 illustrates these details. Figure 3(a) presents the local mesh refinement around the heatsink using a structured quadrilateral mesh. Figure 3(b) shows the global mesh distribution within the L-type domain. The system consists of an aluminum heatsink block placed inside the L-type domain with a velocity inlet and a pressure outlet. Thus, the inlet velocity was set to 1.5 m/s while considering fan power consumption. Velocity-inlet conditions were applied at the inlet, while a no-slip condition was applied on the internal channel surfaces. The entire module was assumed to be adiabatic, with the inlet air temperature fixed at 20°C. The material properties employed in the simulation are shown in Table 2.

Table 2. Material properties

Materials	ρ ($kg \cdot m^{-3}$)	C ($J \cdot kg^{-1} \cdot k^{-1}$)	k ($W \cdot m^{-1} \cdot k^{-1}$)	μ ($g\, m^{-1}\, s^{-1}$)
Aluminum	2719	871	202.4	-
Air	1.16	1006	0.0260	1.83×10^{-5}

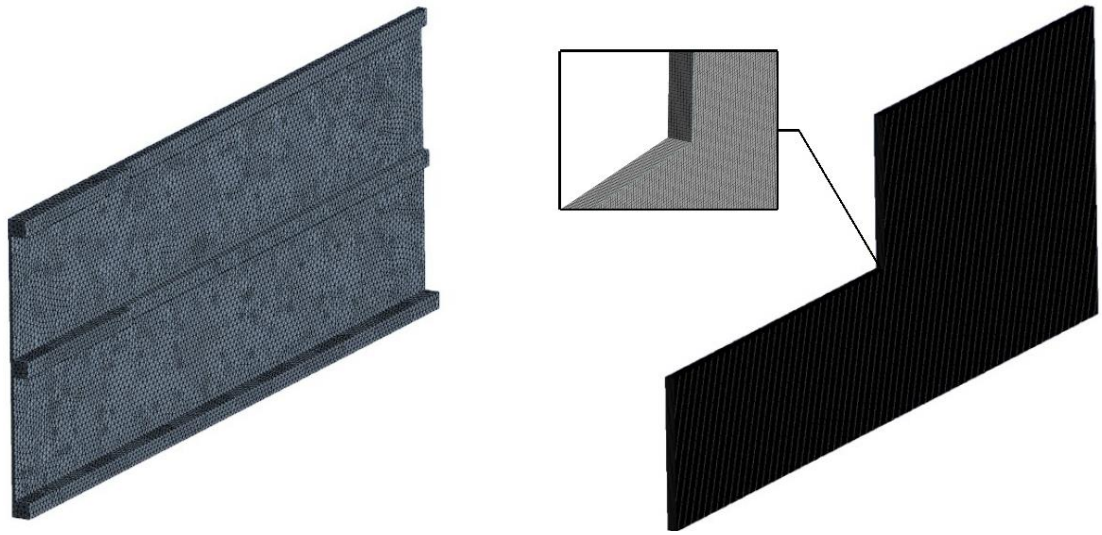

(a) (b)

Figure 3. (a) Local mesh refinement around the heatsink, (b) Global mesh distribution around the L-type domain

C. Grid Independence Test

The accuracy of Computational Fluid Dynamics (CFD) simulations is strongly influenced by the quality of the mesh employed. To ensure model reliability, a grid independence test was conducted using different mesh configurations, where the coarse mesh consisted of 6.666×10^5 elements, the medium mesh consisted of 10^6 elements, and the fine mesh consisted of 1.5×10^6 elements. The Richardson extrapolation technique, generalised by Roache [13], was applied as the methodological basis. Equations (1) and (2) were used to estimate the numerical error for both the coarse and fine mesh cases, while a safety factor of 1.25 was adopted. The relative error values obtained, as presented in Table 3, indicated that mesh refinement affected the convergence index. As illustrated in Figure 4, a higher mesh resolution was associated with improved accuracy. Therefore, the fine mesh configuration was selected for the subsequent simulations.

$$r = \frac{h_2}{h_1} \tag{1}$$

$$\bar{p} = \frac{\ln\left(\frac{f_3 - f_2}{f_2 - f_1}\right)}{\ln(r)} \tag{2}$$

$$GCI_{fine} = \frac{F_s \,|\in|}{\left(r^{\bar{p}} - 1\right)} \tag{3}$$

$$GCI_{coarse} = \frac{F_s \,|\in| \, r^{\bar{p}}}{\left(r^{\bar{p}} - 1\right)} \tag{4}$$

$$\in = \frac{f_{n+1} - f_n}{f_n} \tag{5}$$

$$\frac{GCI_{coarse}}{GCI_{fine} r^{\bar{p}}} \approx 1 \tag{6}$$

$$f\,\mathrm{r}_{h=0} = f_1 + \frac{(f_1 - f_2)}{\left(r^{\bar{p}} - 1\right)} \tag{7}$$

Table 3. Result of grid convergence index

Mesh	Fine	Medium	Coarse
Temperature	33.25466548	33.1533	33.1493
$\bar{\bar{p}}$	7.959651791		
R	1.5		
GCI_{fine}	0.016%		
GCI_{coarse}	0.0006%		
f_{rh}= 0	33.2588514		
$\frac{GCI_{coarse}}{GCI_{fine}r^{\bar{\bar{p}}}}$	1		
Error	0.01259%	0.31733%	0.32942%

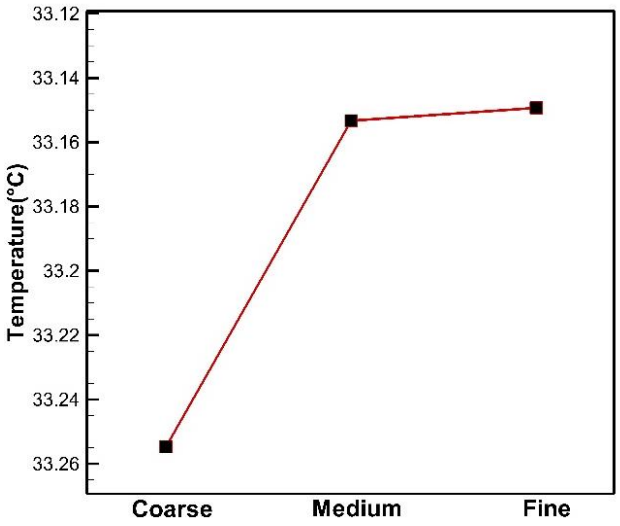

Figure 4. Mesh Sensitivity

D. Governing Equations

To investigate the thermal performance of a cooling system, the study begins by analysing the fluid flow dynamics using the Reynolds-Averaged Navier-Stokes (RANS) equations for continuity and momentum, shown in Eq. (8) and (9) [14]. The k-omega SST model is used to analyse the flow over the boundary, and its mathematical expressions can be found in equations (10) and (11)[15].

$$\frac{\partial \rho}{\partial t} + \frac{\partial}{\partial x_i}(\rho u_i) = 0 \tag{8}$$

$$\frac{\partial}{\partial t}(\rho u_i) + \frac{\partial}{\partial x_i}(\rho u_i u_j) = \frac{\partial p}{\partial x_i} + \frac{\partial}{\partial x_j}\left[\mu\left(\frac{\partial u_i}{\partial x_j} + \frac{\partial u_j}{\partial x_i} - \frac{2}{3}\delta_{ij}\frac{\partial u_i}{\partial x_i}\right)\right] + \frac{\partial}{\partial x_i}\left(-\rho\overline{u_i' u_j'}\right) \tag{9}$$

$$\frac{\partial(\rho k)}{\partial t} + \frac{\partial(\rho U_i k)}{\partial x_i} = P_k - \beta^* \rho\omega k + \frac{\partial}{\partial x_i}\left[\left(\mu + \sigma_k \mu_t\right)\frac{\partial}{\partial x_i}k\right] \tag{10}$$

$$\frac{\partial(\rho\omega)}{\partial(t)} + \frac{\partial(\rho U_i \omega)}{\partial(x_i)} = \alpha\rho S^2 - \beta\rho\omega^2 + \frac{\partial}{\partial x_i}\left[\left(\mu + \sigma_k \mu_t\right)\frac{\partial}{\partial x_i}k\right] + 2(1 - F_1)\sigma_{\omega 2}\frac{1}{\omega}\frac{\partial k}{\partial x_i}\frac{\partial \omega}{\partial x_i} \tag{11}$$

RESULT AND DISCUSSIONS

A. Validation

Figure 5 presents the validation of the computational results against the experimental data reported by Yu Li et al. [9] for the baseplate temperature as a function of flow velocity. As illustrated in Figure 5, both the numerical and experimental results exhibit comparable temperature trends, with only a 7.65% deviation, confirming that the simulation accurately captures the thermal characteristics of the heatsink. The agreement between the experimental measurements and numerical predictions emphasises the reliability of the computational approach in reproducing thermal performance. This consistency demonstrates that the methodology employed is robust, and the validated numerical model can therefore be confidently utilised to investigate further thermal behaviour under different operating conditions.

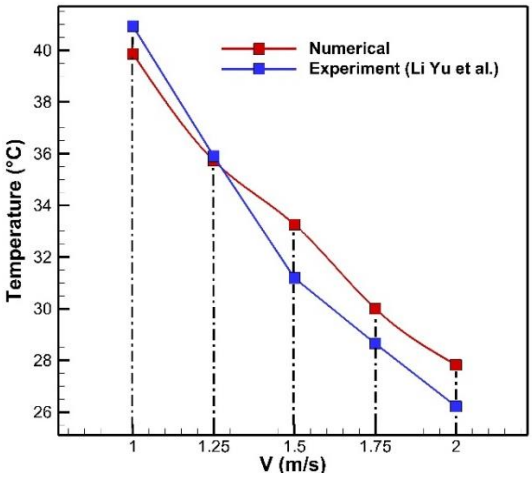

Figure 5. Validation of computational results against experimental data.

B. Analysis

The relationships between excess temperature and pressure drop across the five airflow rates (1–2 m/s), as shown in Figure 6, reveal distinct thermal–hydraulic behaviours for each configuration compared with the baseline case. From the temperature perspective, the baseline configuration shows a gradual decrease in excess temperature as airflow increases because higher inlet velocity intensifies momentum transport near the fin surfaces, thereby thinning the thermal boundary layer and improving convective heat transfer. However, this reduction remains relatively moderate because the flow over the baseline geometry is still dominated by stable boundary-layer development with limited secondary flow generation. Model 1 exhibits a more consistent and slightly steeper temperature decrease than the baseline because the introduced disturbance promotes local recirculation and interrupts boundary-layer growth, allowing cooler air to contact heated regions more effectively, particularly at intermediate flow rates. Model 2 demonstrates a sharper decline in temperature between 1.25 and 1.5 m/s, indicating that the disturbance geometry reaches a flow-transition condition where vortex formation and fluid mixing become stronger, enhancing heat transport from the fin surfaces. Nevertheless, the improvement becomes less significant at higher velocities because the flow begins to stabilize again as inertial effects dominate the local disturbance interaction. Meanwhile, Model 3 shows the most pronounced reduction in excess temperature across all five flow rates, consistently outperforming the baseline and the other models, particularly at higher velocities ($\geq$ 1.5 m/s). This behaviour indicates that the stronger geometric disturbance in Model 3 continuously disrupts the thermal boundary layer, intensifies turbulence production, and increases fluid mixing near the heated surfaces, resulting in the most effective overall thermal performance.

In terms of pressure drop (ΔP), all configurations exhibit a positive correlation with airflow because increasing velocity raises wall friction and form drag within the heatsink channel. The baseline maintains a moderate ΔP increase, serving as a reference. Model 1 shows a slightly higher ΔP because the additional disturbance induces local flow separation and recirculation, producing a trade-off between improved heat transfer and increased resistance. Model 2 presents a comparable or slightly lower ΔP at lower velocities but rises more significantly at higher flow rates as stronger vortex interaction increases momentum loss. Model 3, however, exhibits the highest ΔP among all configurations, especially above 1.5 m/s, because the intense turbulence and repeated flow disruption create substantial aerodynamic losses. Therefore, although Model 3 delivers the best cooling performance, Model 2 can be considered the optimal configuration overall due to its more favorable balance between enhanced convective heat transfer and manageable pressure drop across the tested flow conditions under the investigated operating conditions.

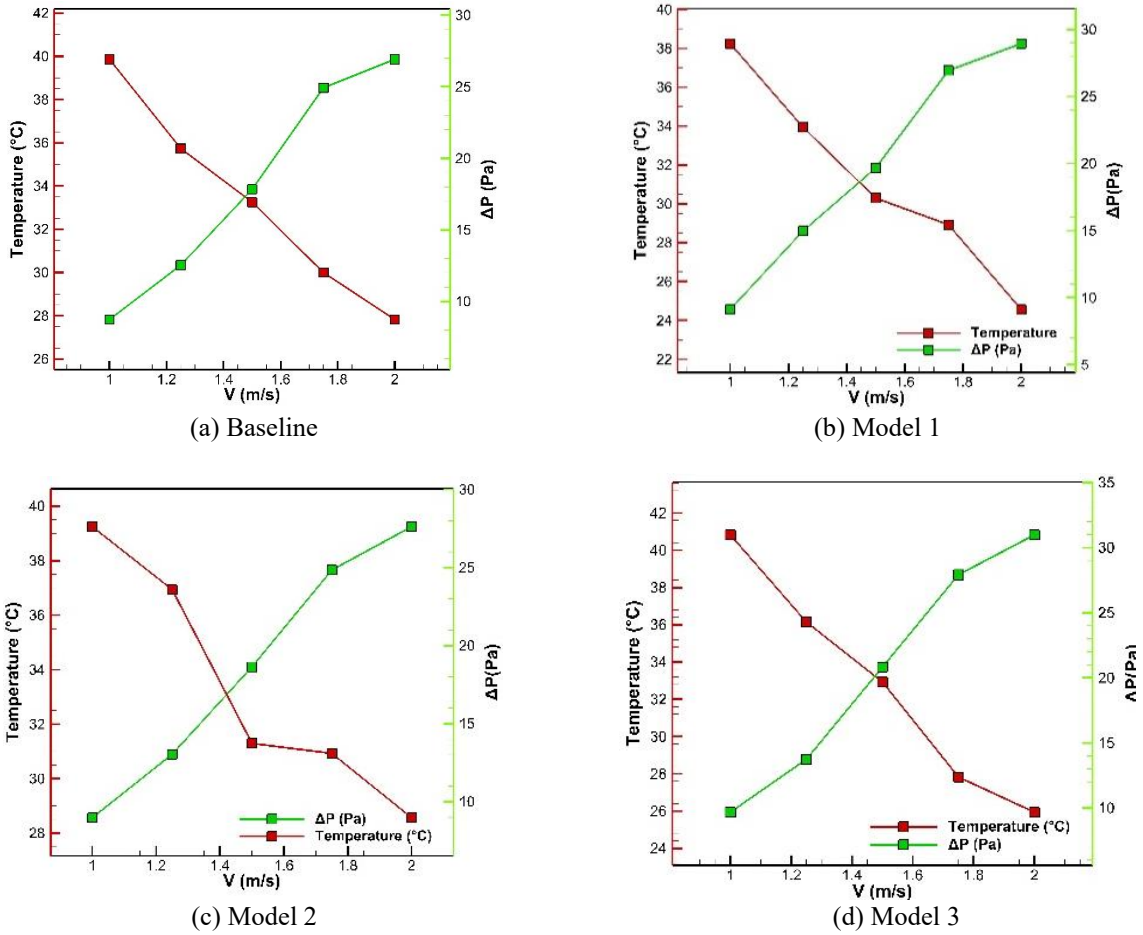

(a) Baseline (b) Model 1

(c) Model 2 (d) Model 3

Figure 6. Temperature and Pressure differences of the models.

Figure 7 illustrates the temperature contour distributions for all configurations at V = 1.5 m/s, emphasizing how geometric disturbances influence the thermal behavior of the heatsink. In the baseline case, the temperature field remains relatively stratified, with smooth and nearly parallel isotherms indicating minimal flow disturbance. The thermal boundary layer develops steadily along the heated surface, leading to a concentrated high-temperature region near the bottom wall and suggesting limited convective heat transfer. When internal structures are introduced, the thermal patterns begin to change. In Model 1, the circular obstacles slightly perturb the flow, as seen from the mild bending of the isotherms around the structures. This reflects the onset of weak recirculation zones, which provide a small degree of mixing and only a marginal reduction in the thermal boundary layer thickness, resulting in a temperature distribution still similar to the baseline.

In Model 2, the presence of square geometries leads to stronger flow disruption due to sharper edges, producing more noticeable deformation of the temperature contours. This indicates enhanced mixing compared to Model 1, with a more distributed temperature field and a moderate reduction in localized high-temperature regions near the heated surface. However, the improvement remains limited, as warmer zones are still clearly visible. In contrast, Model 3 shows a different trend. Although the octagonal structures generate significant disturbance and complex contour deformation, the temperature field reveals a wider spread of higher temperatures, particularly near the lower region. Overall, the results indicate that increasing geometric complexity does not necessarily improve thermal performance under these conditions. While Models 1 and 2 provide slight enhancements in mixing, Model 3 exhibits less effective heat removal, as indicated by the broader high-temperature distribution. Therefore, Model 2 demonstrates the most balanced thermal behavior among the modified configurations, followed by Model 1, while Model 3 performs the least effectively.

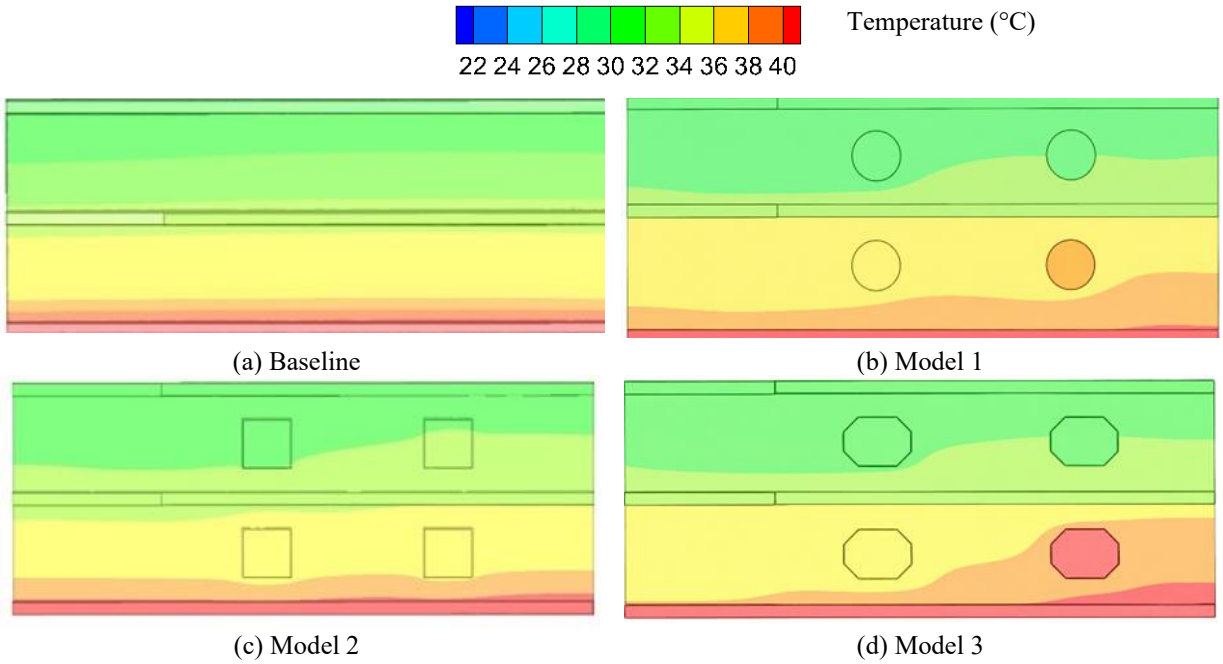

Figure 7. Heatsink Contour

Figure 8 presents the three-dimensional temperature distribution within the computational domain at V = 1.5 m/s, providing a clearer representation of the airflow behavior and heat-transfer characteristics compared with the contour distribution shown previously in Figure 7. In the baseline configuration, the airflow remains relatively uniform and stratified, with limited interaction between the upper cold-air region and the lower heated surface. This condition produces weak air homogenization because the cooler air mainly flows through the upper channel, while the hotter fluid remains concentrated near the bottom wall. Consequently, convective heat transfer becomes less effective because the stable thermal boundary layer suppresses momentum exchange and limits thermal-energy transport from the heated surface to the bulk airflow. The absence of significant flow disturbance also minimizes vortex formation, causing the thermal field to remain localized near the heat source and resulting in inefficient heat dissipation. In Model 1, the introduction of circular obstacles begins to disrupt the uniform flow structure. The airflow experiences localized deviation and mild recirculation around the obstacles, partially interrupting the thermal boundary layer and promoting limited mixing between hot and cold fluid regions. This mechanism improves air homogenization by allowing cooler air to penetrate closer to the heated wall. However, the generated vortices remain relatively weak and spatially confined, so the hot region near the heated surface is still concentrated within the lower section of the channel. As a result, the enhancement in convective heat transfer remains modest and produces only a slight improvement in overall thermal performance.

Model 2 exhibits a more significant improvement in airflow homogenization and thermal transport. The square geometries induce stronger flow separation and more stable recirculation zones, intensifying momentum exchange between fluid layers. This phenomenon enables cooler air to reach the heated surface more effectively while simultaneously transporting heated fluid away from the wall region. The resulting increase in turbulent mixing reduces thermal stratification and produces a more uniformly distributed temperature field throughout the computational domain. From a convective heat-transfer perspective, this configuration improves thermal-energy extraction more efficiently than Model 1, as indicated by the reduced concentration of high-temperature regions and the stronger interaction between the core airflow and the heated surface.In contrast, Model 3 generates the strongest flow disturbance but not the most effective heat-transfer performance. Although the octagonal structures produce intense mixing and complex recirculation patterns, the temperature field indicates that heated fluid is redistributed within the domain rather than effectively removed downstream. Excessive flow disruption increases local flow resistance and prolongs the residence time of heated air near the lower region, causing thermal accumulation and a wider spread of elevated temperatures. Therefore, despite the higher mixing intensity, Model 3 results in less efficient heat dissipation than Model 2, indicating suboptimal thermal-management performance.

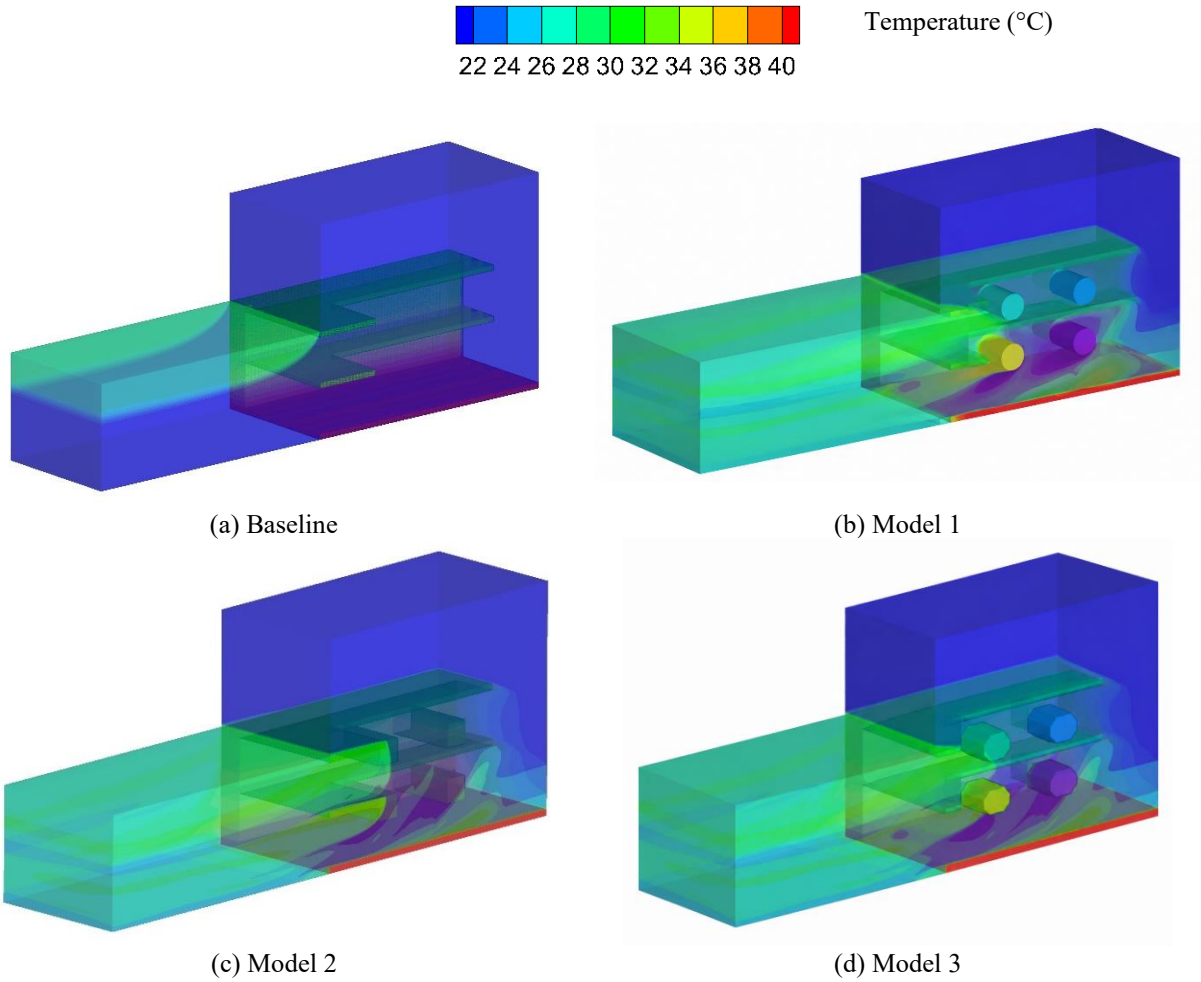

Figure 8. Domain Contour

CONCLUSION

This study numerically investigated the effect of flow-disturbance geometry on the thermal–hydraulic performance of a forced air-cooled heatsink under a constant heat-flux condition. The results demonstrate that the introduction of internal geometric disturbances significantly alters the airflow structure, temperature distribution, and overall convective heat-transfer behaviour. From a quantitative perspective, Model 3 consistently achieved the lowest excess temperature across the tested velocity range (1–2 m/s), indicating the highest cooling capability. However, this improvement was accompanied by the largest pressure drop (ΔP), especially at higher velocities (≥ 1.5 m/s), reflecting a substantial increase in flow resistance and energy consumption. In contrast, Model 1 provided only a slight reduction in temperature compared to the baseline, with a relatively small increase in ΔP, indicating limited enhancement in thermal performance. Model 2 exhibited a more balanced thermal–hydraulic behaviour within the intermediate velocity range (1.25–1.5 m/s) while maintaining a moderate pressure drop. This indicates that Model 2 achieves a favourable compromise between enhanced convective heat transfer and acceptable aerodynamic penalty. Overall, although Model 3 delivered the best cooling performance in terms of temperature reduction, its high pressure drop makes it less efficient for practical applications. Model 2 was identified as the optimal configuration, offering the best trade-off between thermal enhancement and energy efficiency, supported by both quantitative data and qualitative flow behaviour.

REFERENCES

[1] T.-Y. Kuo, S.-C. Wong, C.-C. Hsu, and C.-Y. Lu, “Numerical and experimental study on UTVC/plate-fin heatsink modules with an axial impingement fan,” *Int. Commun. Heat Mass Transf.*, vol. 171, p. 110173, 2026.

[2] J. Jiao, Y. Li, L. Gong, and F. Duan, "Enhanced thermal performance of a hybrid air and liquid cooling system for high power data center servers," *Appl. Therm. Eng.*, vol. 283, p. 128878, 2026, doi: https://doi.org/10.1016/j.applthermaleng.2025.128878.

[3] A. G. Mohammed, H. Hasini, K. E. Elfeky, Q. Wang, M. A. Hajara, and N. I. Om, "Cooling effectiveness enhancement of parallel air-cooled battery system through integration with multi-phase change materials," *Int. J. Therm. Sci.*, vol. 201, p. 109030, 2024, doi: https://doi.org/10.1016/j.ijthermalsci.2024.109030.

[4] W. Liang *et al.*, "Optimization design of proton exchange membrane fuel cell cooling plate based on dual-objective function topology theory," *Int. Commun. Heat Mass Transf.*, vol. 153, p. 107404, 2024.

[5] N. S. Mane *et al.*, "Hybrid phase change material techniques for battery thermal management in electric vehicles: A comprehensive review and bibliometric analysis," *Energy Reports*, vol. 14, pp. 4415–4436, 2025, doi: https://doi.org/10.1016/j.egyr.2025.11.024.

[6] E. Ermadani *et al.*, "NUMERICAL STUDY ON THERMAL PERFORMANCE OF MINI-CHANNEL COOLING ON CYLINDRICAL LITHIUM-ION BATTERY COOLING SYSTEM," *Log. J. Ranc. Bangun dan Teknol.*, vol. 26, no. 1, pp. 86–94, 2026.

[7] C.-C. Wang, "A quick overview of compact air-cooled heat sinks applicable for electronic cooling—recent progress," *Inventions*, vol. 2, no. 1, p. 5, 2017.

[8] K. Mankani, H. N. Chaudhry, and J. K. Calautit, "Optimization of an air-cooled heat sink for cooling of a solar photovoltaic panel: A computational study," *Energy Build.*, vol. 270, p. 112274, 2022.

[9] S. Caliskan, F. Guler, and S. S. Seyitoglu, "Investigating the cooling performance of CPU heat sinks using Al2O3/Water and SiC/water nanofluids," *Int. J. Therm. Sci.*, vol. 226, p. 110849, 2026.

[10] J. Mustafa, M. M. Abdullah, M. Z. Ahmad, S. Husain, and M. Sharifpur, "Numerical study of two-phase turbulence nanofluid flow in a circular heatsink for cooling LEDs by changing their location and dimensions," *Eng. Anal. Bound. Elem.*, vol. 149, pp. 248–260, 2023.

[11] E. Cuce, P. M. Cuce, and T. Guclu, "A novel passive cooling configuration for photovoltaic panels based on bio-inspired heatsinks and nanoparticle-enhanced PCM," *Appl. Therm. Eng.*, p. 130312, 2026.

[12] Y. Li, H. Fan, and Y. Jiu, "Investigation of a hybrid two-layered channel-jet heat sink for air cooling," *Int. J. Therm. Sci.*, vol. 203, p. 109121, 2024.

[13] P. J. Roache, "Perspective: a method for uniform reporting of grid refinement studies," 1994.

[14] S. M. A. Aftab, A. S. Mohd Rafie, N. A. Razak, and K. A. Ahmad, "Turbulence model selection for low Reynolds number flows," *PLoS One*, vol. 11, no. 4, p. e0153755, 2016.

[15] L. Rong, X.-S. Bai, J.-C. Li, R.-Z. Zhang, and W.-W. Yang, "Design and optimization of a hybrid cooling configuration combining PCM and liquid cooling for Li-ion battery using data-based response surface approximation model," *Appl. Therm. Eng.*, vol. 245, p. 122844, 2024.